Physical Reservoir Computing for Real-Time Electrocardiogram Arrhythmia Detection Through Controlled Ion Dynamics in Electrochemical Random-Access Memory

Kyumin Lee, Dongmin Kim, Jongseon Seo, and Hyunsang Hwang*

From the perspective of developing low-power mobile healthcare devices capable of real-time electrogram diagnosis, memristor-based physical reservoir computing (PRC) offers a promising alternative to conventional deep neural network (DNN)-based systems. Here, real-time electrocardiogram (ECG) monitoring and arrhythmia detection are demonstrated using electrochemical random-access memory (ECRAM)-based PRC. ECRAM devices provide the millisecond-range temporal resolution required for bio-potential signals like ECG. Through material and process engineering, it is identified that higher ionic conductivity (σ_{ion}) in the electrolyte layer and lower ionic diffusivity (D_{ion}) in the channel layer are crucial for achieving non-linear dynamics and fading memory characteristics. In addition, LaF_3/WO_x-based ECRAM exhibits low-power operation ($\approx$300 pW spike^{-1}) with minimal cycle-to-cycle (CTC) variation (<10%). Arrhythmia detection tests confirmed the feasibility of real-time ECG monitoring, achieving a high classification accuracy of 93.04% with a 50-fold reduction in training parameters compared to DNN-based systems. Therefore, the developed LaF_3/WO_x-based ECRAM with engineering guidelines of ion dynamics makes a significant contribution to mobile healthcare systems for electrogram diagnosis.

1. Introduction

With the advent of the big data era, the demand for efficient data processing methods has grown rapidly across various fields. In healthcare applications, continuous monitoring of patients' electrograms using wearable electronic devices has become essential for early diagnosis and disease prevention.[1,2] Electrogram, characterized by continuously fluctuating time-series data, enables the detection of abnormal waveforms indicative of various health problems. For example, real-time analysis of electrocardiogram (ECG) signals, which represent the electrical activity of the human heart, facilitates the detection of arrhythmia.[3,4] While recent studies have demonstrated high-accuracy ECG classification using deep neural network (DNN)-based systems, the high computational power and energy demands of these systems limit their feasibility for mobile environments.[5–7] Since arrhythmia can arise unexpectedly during daily life, continuous real-time ECG monitoring via mobile devices is critical for timely diagnosis. Therefore, developing low-power hardware systems that can serve as alternatives to the DNN-based model is crucial.

Reservoir computing (RC) is an advanced computing paradigm that emerged in the early 2000s, with an architecture well-suited for adaptively learning spatiotemporal features and hidden patterns in complex time-series data.[6–10] An RC system typically consists of three layers: input, reservoir, and output. The reservoir layer, composed of a fixed recurrent network, maps input temporal signals into a high-dimensional feature space through non-linear transformations, while the output layer processes this data with a linear classifier to produce the final result. Only the weights between the reservoir and output layers are trained, enabling RC systems to analyze data efficiently with far fewer training parameters than DNN-based architectures. Furthermore, the fixed random structure of the reservoir layer provides strong adaptability to new data, allowing previously trained models to handle new scenarios without modification. These attributes make RC's low-power consumption, low cost, and high accuracy in real-time temporal data processing ideal for mobile healthcare applications.

To implement RC architecture in mobile sensors, the reservoir layer must be realized in hardware using physical devices. This approach, known as physical reservoir computing (PRC), can be categorized into four main types: delay-coupled RC, in-material

K. Lee, D. Kim, J. Seo, H. Hwang
Center for Single Atom-based Semiconductor Device and the
Department of Materials Science and Engineering
Pohang University of Science and Technology
Pohang 37673, Republic of Korea
E-mail: hwanghs@postech.ac.kr

**ADVANCED
SCIENCE NEWS**

www.advancedsciencenews.com

**ADVANCED
ELECTRONIC
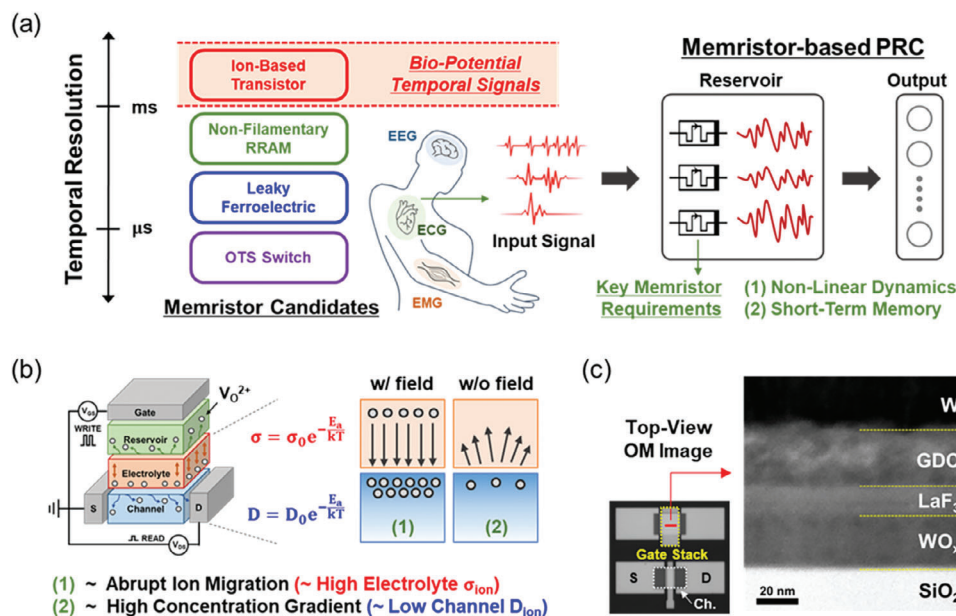MATERIALS**

www.advelectronicmat.de

Figure 1. Introduction to ECRAM-based PRC. A) Concept of a real-time health monitoring system utilizing memristor-based PRC. The non-linear dynamics and millisecond-scale fading memory characteristics of memristor reservoir nodes enable real-time monitoring of bio-potential temporal signals such as EEG, ECG, and EMG. B) Schematic illustration of the ECRAM structure and its requirements for non-linearity and tunable STM characteristics. Optimizing ion dynamics requires high σ_{ion} in the electrolyte layer and low D_{ion} in the channel layer. C) Top-view OM image and cross-sectional TEM image of the fabricated ECRAM devices for PRC applications.

RC, rotating neuron-based RC, and dynamic memristor-based RC.[8–14] Delay-coupled RC generates dynamic responses using a single node, simplifying physical implementation but relying on time multiplexing for serial processing, which limits processing speed.[11] In-material RC uses intrinsic dynamic responses of materials for high-dimensional mappings, enabling simplified designs and reduced costs but facing challenges in memory capacity and signal flow control.[12] Rotating neuron-based RC employs physically rotating nodes to create recurrent structures, reducing system complexity but complicating planar hardware layouts.[13] Dynamic memristor-based RC leverages memristor devices with short-term memory (STM) and non-linear dynamics as reservoir nodes, simplifying hardware implementation but with limited processing in long-term information.[14] For mobile ECG monitoring, where input signals are typically short (on the millisecond scale) and require simple hardware design, dynamic memristor-based RC is the most suitable option.

Recent studies have explored emerging electronic devices such as non-filamentary resistive random-access memory (RRAM),[14,15] ovonic threshold switch (OTS),[16] and leaky ferroelectric memory[17] as reservoir nodes in dynamic memristor-based RC implementations. These devices have demonstrated feasibility in diverse applications such as gesture[14] and spoken digit recognition[15,16] by leveraging unique device properties. However, due to their inherent switching mechanisms, these devices face limitations for practical applications including poor cycle-to-cycle uniformity[16] and high power consumption.[15,17] In healthcare applications, bio-potentials like ECG, electroencephalography (EEG), and electromyography (EMG) signals have filtering frequencies ranging from 0.05 to 2000 Hz, requiring temporal resolution in the millisecond range.[18] However, the retention times of the aforementioned devices, typically below the microsecond range, are insufficient for these applications, as shown in **Figure 1a**.

Electrochemical random-access memory (ECRAM), which operates via ion redox reactions inspired by battery principles, provides a promising solution to these challenges. ECRAM devices exhibit excellent reliability and state richness due to uniform ion transport during switching.[19–28] Low-energy operation can be achieved by using high-resistance electrolyte and channel materials.[19–23] Furthermore, CMOS compatibility can be ensured using oxygen ion conductors as electrolytes and transition metal oxides as channel materials.[24–28] Traditionally, ECRAM research has focused on improving linearity and retention characteristics for their application as synaptic elements in DNN-based systems. Building on these findings, the non-linearity required for PRC reservoir nodes and tunable retention characteristics in the millisecond range can be achieved through material and process optimization in ECRAM devices. In our previous studies, we demonstrated that low ionic conductivity (σ_{ion}) in the electrolyte layer is a key parameter for achieving ideal linearity in ECRAM devices, as supported by experimental results and ion distribution simulations.[26–28] Specifically, when σ_{ion} is high, abrupt ion migration occurs during the voltage gating process, leading to non-linear weight updates that are desirable for ECRAM reservoir nodes. Additionally, we found that retention characteristics are primarily influenced by the concentration gradient between the electrolyte and channel layers.[22] This suggests that adjustable retention could be achieved by controlling D_{ion} in the channel layer. Lower D_{ion} in the channel layer is expected to cause greater ion accumulation at the channel-side interface during voltage gating, resulting in degraded retention due to a larger ion concentration gradient.

**ADVANCED
SCIENCE NEWS**

www.advancedsciencenews.com

**ADVANCED
ELECTRONIC
MATERIALS**

www.advelectronicmat.de

In this report, we present a power-efficient ECRAM-based PRC for real-time ECG monitoring. By introducing LaF$_3$ with high σ_{ion} as the electrolyte layer, we achieved the non-linearity and STM characteristics required for PRC reservoir nodes. Furthermore, tunable time constants in the millisecond range, compatible with ECG signals, were successfully achieved through D$_{ion}$ engineering of the WO$_x$ channel via stoichiometry control. Leveraging these optimized LaF$_3$/WO$_x$-based ECRAM properties, we performed arrhythmia diagnosis tests using an ECG dataset, achieving a high accuracy rate of 93.04%. Our proposed LaF$_3$/WO$_x$-based ECRAM, with parameter engineering guidelines, demonstrates significant potential for applications in PRC-based mobile healthcare devices for electrogram detection.

2. Results and Discussion

To implement a PRC system for ECG signal processing, ECRAM devices serving as memristor nodes must exhibit non-linear weight updates and short retention characteristics within the millisecond range (Figure 1a). The weight update linearity and retention characteristics of ECRAM devices are significantly influenced by the σ_{ion} of the electrolyte and the D$_{ion}$ of the channel layer,[22,26–28] as shown in Figure 1b. Therefore, controlling these two key parameters is necessary for ECRAM-based PRC applications.

A high σ_{ion} in the electrolyte allows a large number of ions to move rapidly when a gating pulse is applied. This results in abrupt changes in channel conductance, facilitating the non-linear dynamics required for PRC.[28] Additionally, this rapid ionic movement creates a significant concentration gradient at the interface between the channel and electrolyte layers, leading to substantial ion back-diffusion and consequently shorter retention times.[22] Regarding the D$_{ion}$ in the channel layer, previous studies have shown that lower D$_{ion}$ causes ions injected by gating pulses to accumulate near the electrolyte/channel interface.[23,27] At this point, a significant concentration gradient forms at the interface, contributing to a shorter retention time. Thus, achieving the non-linear dynamics and STM characteristics required for ECRAM reservoir nodes necessitates an electrolyte with high σ_{ion} and a channel with low D$_{ion}$.

A schematic diagram of the ECRAM device is shown in Figure 1b. ECRAM devices operate based on the migration of various ions; in this study, an oxygen ion (or oxygen vacancy) based ECRAM (O-ECRAM) was developed to ensure compatibility with the CMOS process.[24–28] The device comprises a 10 mol% Gd-doped CeO$_2$ (Gd$_{0.1}$Ce$_{0.9}$O$_{1.95}$, GDC) as the reservoir layer, HfO$_2$ or LaF$_3$ as the electrolyte layer, and WO$_x$ as the channel layer. The GDC reservoir layer provides a source of oxygen vacancies within the O-ECRAM device. As the number of ions participating in the switching process increases, the range of conductance changes, contributing to state richness, also increases. In addition, the concentration gradient at the electrolyte/channel interface intensifies after voltage gating, resulting in shorter retention times. In the field of solid oxygen fuel cells, GDC is well-known as a material capable of supplying sufficient oxygen vacancies for ionic conduction,[29,30] making it an ideal reservoir layer for O-ECRAM devices. HfO$_2$ is a representative material used in RRAM, operating through oxygen vacancy migration, and is widely used as an electrolyte material in O-ECRAM.[24,28] LaF$_3$ is

commonly employed in oxygen sensors as an oxygen ion conductor that functions at room temperature due to its high σ_{ion}.[31] To investigate the effect of electrolyte σ_{ion} on ECRAM characteristics, HfO$_2$ and LaF$_3$ were selected for comparison as electrolyte layers. WO$_x$, which offers a wide range of conductance (from pS to mS) depending on ion doping concentration, was chosen as the channel material.[20–28] Additionally, the switching behavior of ECRAM devices can be tuned by controlling the D$_{ion}$ in WO$_x$ through stoichiometry adjustments.[27,28] To understand the effect of D$_{ion}$ on retention characteristics, WO$_x$ with various stoichiometries was introduced by adjusting the oxygen gas flow rate during reactive sputtering. Figure 1c presents the top-view OM image and cross-section TEM image of the LaF$_3$/WO$_x$-based ECRAM devices for PRC applications.

To extract the σ_{ion} and barrier energy for ion conduction (E$_{a,ion}$) in the electrolyte layer, temperature-dependent electrochemical impedance spectroscopy (EIS) measurements were performed for HfO$_2$ and LaF$_3$, as shown in **Figure 2a,b**, respectively.[28] A two-terminal metal-electrolyte-metal structure with inert Pt electrodes was used for the EIS analysis to measure the intrinsic σ_{ion} of the electrolyte materials. The Debye equivalent circuit applied to the Nyquis plot, with R$_s$, R$_{ion}$, and a constant phase element (CPE) as components, is shown in the inset of Figure 2b. R$_s$ represents the sum of the resistances from the electrolyte, electrodes, and contacts, while R$_{ion}$ corresponds to the ionic resistance of the electrolyte. The CPE accounts for the bulk/geometrical capacitance of the electrolyte. In this configuration, σ_{ion} can be calculated as the inverse of R$_{ion}$, with its value can be extracted from the point where the semicircle in the Nyquist plot intersects the axis of real impedance (Re[Z]).[32] The σ_{ion} can be expressed as follows:[33]

$$\sigma_{ion}T = \sigma_0 \exp\left(-E_{a,ion}/k_BT\right) \tag{1}$$

where T is the measurement temperature, σ_0 is the temperature-independent pre-factor, and k$_B$ is the Boltzmann constant. Consequently, E$_{a,ion}$ can be extracted from the slope of the Arrhenius plot of σ_{ion}T, as shown in Figure 2c. The results confirm that LaF$_3$ exhibits a σ_{ion} approximately ten times higher than that of HfO$_2$ and a lower E$_{a,ion}$ (0.34 eV in HfO$_2$, 0.14 eV in LaF$_3$).

Introducing the LaF$_3$ electrolyte with high σ_{ion} into the O-ECRAM device facilitates the realization of non-linear weight update behavior due to rapid ion migration during voltage gating. This is demonstrated by the weight update curves of O-ECRAM devices with HfO$_2$ and LaF$_3$ electrolytes, as shown in Figure 2d,e, respectively. For a fair comparison, all layers except the electrolyte layer were kept consistent, with GDC as the reservoir, WO$_{2.3}$ as the channel material, and identical layer thickness for both devices. As a result, the LaF$_3$-based ECRAM exhibits non-linear weight update behavior, achieving a conductance change of $\approx$30 μS, similar to the HfO$_2$-based ECRAM, but requiring a lower write pulse amplitude (+3.0 V for LaF$_3$ compared to +5.0 V for HfO$_2$). Furthermore, retention comparison tests indicate that the LaF$_3$-based ECRAM meets the STM requirements, as shown in Figure 2f. This can be attributed to the more significant ion concentration gradient formed at the electrolyte/channel interface in the LaF$_3$-based ECRAM, driven by the rapid ion migration within the LaF$_3$ electrolyte during voltage gating. In summary, to achieve non-linear dynamics and STM characteristics required for PRC
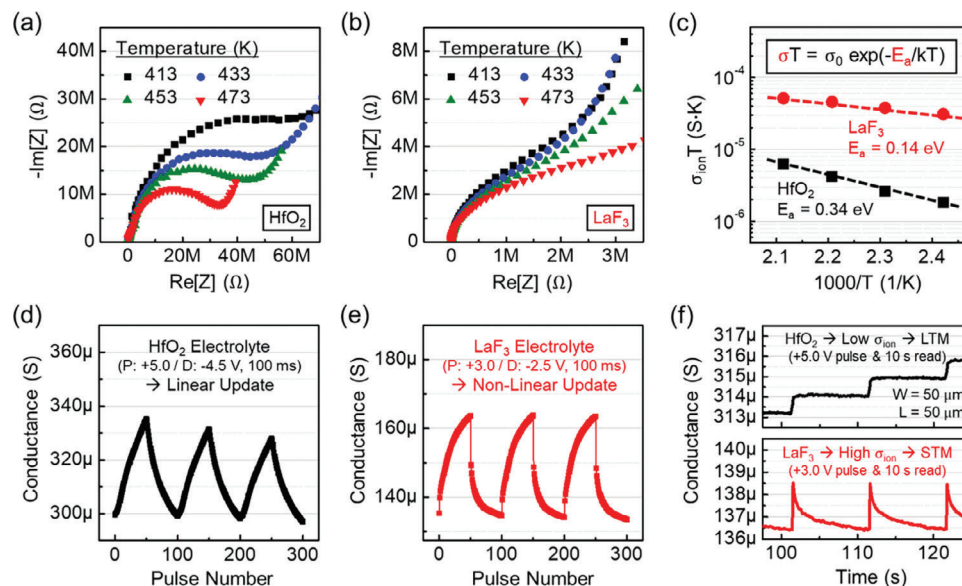
Figure 2. Electrolyte material engineering for non-linear dynamics and fading memory. A,B) EIS analysis and C) Arrhenius plot of $\sigma_{ion}T$ at various measurement temperatures for HfO_2 and LaF_3 electrolytes. LaF_3 demonstrates higher σ_{ion} and lower $E_{a,ion}$ compared to HfO_2, indicating more rapid ion migration under voltage gating. D,E) Synaptic weight update curves and F) fading memory properties of HfO_2- and LaF_3-based ECRAM devices with the same $WO_{2.3}$ channel. Non-linear weight update and STM characteristics are successfully achieved using the LaF_3 electrolyte.

applications, the electrolyte layer must exhibit high σ_{ion}, and LaF_3 proves to be a suitable material for this purpose.

To accommodate various forms of ECG signals, the memristor used as a reservoir node must exhibit diverse retention times. Therefore, it is crucial to identify the key parameter that determines the retention characteristics of ECRAM. As mentioned earlier, a smaller D_{ion} in the WO_x channel layer is expected to create a greater ion concentration gradient at the electrolyte/channel interface, resulting in shorter retention times. This can be achieved by controlling the stoichiometry of WO_x, and the D_{ion} in the WO_x channel layer can be extracted through cyclic voltammetry (CV) analysis performed by sweeping voltage between the gate and source electrodes in the ECRAM structure.[23,27] **Figure 3a,b** show the CV analysis results for LaF_3-based ECRAM devices with O-less ($WO_{2.3}$) and O-rich ($WO_{2.9}$) channels, respectively. All CV analysis results for various WO_x stoichiometries are shown in Figure S1 (Supporting Information). The peak currents (I_{peak}) observed under all WO_x stoichiometry conditions represent the electrochemical reactions of WO_x driven by reversibly doped O ions.[34] According to the Randles-Sevick equation, D_{ion} is proportional to the square of the slope of the linear I_{peak}-square root of the voltage scan rate (v) curve, expressed as follows:[27,28]

$$I_{paek} = 0.4958(Fn)^{3/2}(RT)^{-1/2}AC_{ion}(\beta D_{ion}v)^{1/2} \quad (2)$$

where F is the Faraday constant, n is the charge transfer number, R is the gas constant, A is the active device area, C_{ion} is the ion concentration, and β is the transfer coefficient. Figure 3c shows the linear I_{peak}-$v^{1/2}$ fittings for all WO_x stoichiometry conditions. Assuming F, n, R, T, A, C_{ion}, and β are identical across all conditions, D_{ion} can be indirectly compared using the slope values. As

a result, a wide D_{ion} range of $\approx \times 100$ was achieved between $WO_{2.3}$ and $WO_{2.9}$.

Figure 3d shows the weight update behaviors and STM characteristics of LaF_3-based ECRAM devices with $WO_{2.3}$ and $WO_{2.9}$ channel layers. The time constant, extracted from the fitting of an exponential decay function, was used to compare the STM characteristics. As a result, the time constant for the stoichiometric $WO_{2.9}$ channel (42.2 ms) was found to be ten times shorter than that of the sub-stoichiometric $WO_{2.3}$ channel (621.7 ms). This confirms that the D_{ion} of the channel layer is a key parameter determining the retention time, as previously discussed. All results for weight update curves and STM characteristics across WO_x stoichiometry conditions are summarized in Figures S2 and S3 (Supporting Information), respectively. As the WO_x composition approaches stoichiometry, non-linearity is maintained while the retention time decreases. Figure 3e shows the time constants for all conditions, demonstrating that tunable temporal resolution within the millisecond range is achievable. Consequently, the LaF_3/WO_x-based ECRAM device is well-suited for diverse ECG signal processing applications using PRC. Moreover, by further widening the range of WO_x stoichiometry control, an even broader range of time constants can be obtained, providing greater flexibility in tailoring retention characteristics to meet specific signal processing requirements.

For fast data processing in the memristor-based PRC system, the response delay of the reservoir node to external signals must be minimized. In other words, the write speed of the ECRAM device should be fast. To evaluate the operation speed of the proposed LaF_3/WO_x-based ECRAM device, the ΔG trends under various pulse width and pulse amplitude conditions were analyzed, as shown in Figure S4 (Supporting Information). Similar to conventional ion-based ECRAMs, ΔG increases linearly with pulse width and exponentially with pulse amplitude, indicating

**ADVANCED
SCIENCE NEWS**

www.advancedsciencenews.com
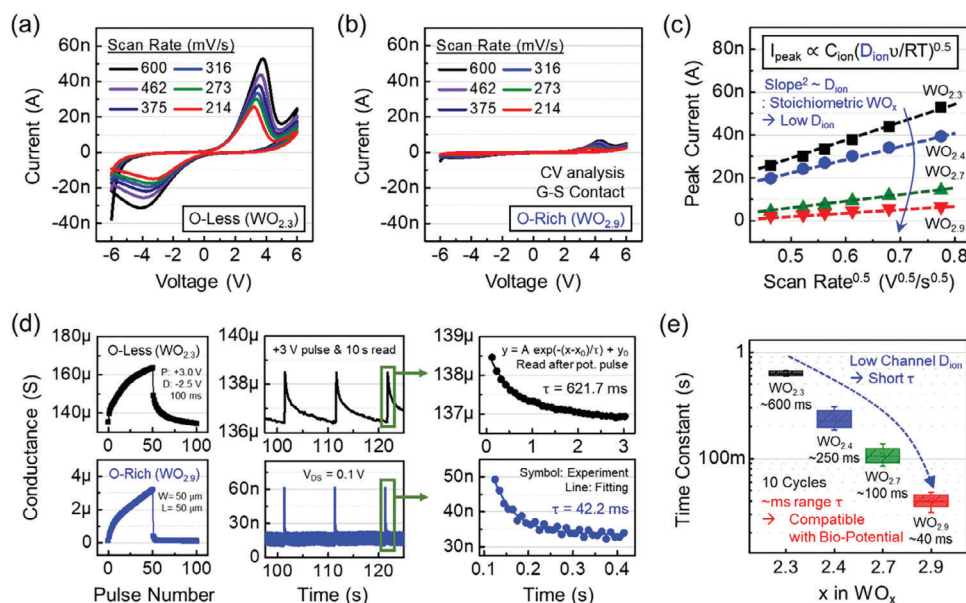
**ADVANCED
ELECTRONIC
MATERIALS**

www.advelectronicmat.de

Figure 3. Channel stoichiometry engineering for tunable STM characteristics. A,B) CV analysis and B) linear fitting of I_{peak}-$v^{1/2}$ for WO_x channels with various stoichiometries. The WO_x channel demonstrates higher D_{ion} as it becomes more sub-stoichiometric. D) Synaptic weight update curves and fading memory properties of the LaF_3-based ECRAM devices with O-less ($WO_{2.3}$) and O-rich ($WO_{2.9}$) WO_x channels. E) Time constants extracted from the conductance decay of LaF_3-based ECRAM devices with various WO_x channel stoichiometries. Tunable STM within the millisecond range is achieved in the LaF_3/WO_x stack.

that the operating mechanism of LaF_3/WO_x-based ECRAM involves field-induced ion migration and electrochemical reversible ion doping.[35,36] The results show that a pulse width of several tens of miliseconds is required for a 3.0 V pulse amplitude. Increasing the pulse amplitude can effectively reduce the delay; however, additional approaches are required to further enhance the write speed. In our previous research, it was reported that reducing the channel area improves the operation speed of ECRAM by reducing the RC delay.[27] A similar trend is observed in the proposed LaF_3/$WO_{2.7}$-based ECRAM device, as shown in **Figure 4**a,b. Therefore, if device scaling to the nanometer scale can be implemented, delays shorter than the microsecond range can be achieved.

Channel area scaling also offers advantages in terms of energy efficiency by reducing gate leakage. The energy consumption for write and read operations in the LaF_3/$WO_{2.7}$-based ECRAM device was calculated at V_{GS} of 3 V and V_{DS} of 0.1 V, as shown in Figure 4c. It consumes $\approx$30 pJ spike^{-1} of write energy ($\approx$300 pW spike^{-1} of power) with a device size of 100 μm^2 (W = 10 μm, L = 10 μm) and a pulse width of 100 ms. Further scaling of the channel area and pulse width allows the device to meet the biological energy requirements of less than 10 fJ spike^{-1}.

Reliable device performance is essential for achieving high classification accuracy in PRC operations. The endurance test for the LaF_3/$WO_{2.7}$-based ECRAM device was performed for 50 cycles with 50 potentiation and depression states per cycle, using up to 5 × 10^4 write pulses with an amplitude of +3.0 V/-2.5 V and a width of 100 ms (Figure 4d). As a result, reliable cycling characteristics with no conductance degradation were observed. Figure 4e demonstrates the cycle-to-cycle (CTC) variation characteristics extracted from

the endurance test, indicating excellent uniformity within 10%.

To evaluate the pattern recognition capability of the proposed ECRAM device, its current response to a pulse train was analyzed. For example, the digit image "P" can be divided row-wise into [1110], [1010], [1110], and [1000], which can be distinguished by applying different voltage inputs for 1 and 0 (Figure 4f). Figure 4g shows the current responses of the LaF_3/$WO_{2.7}$-based ECRAM device for 16 different states, ranging from [0000] to [1111]. Write pulses of +3.0 and +0.5 V were applied for 1 and 0, respectively, and current changes were monitored using a 0.1 V read pulse. The result indicates that the 16 states were successfully distinguished. In practical applications, real-time repetitive ECG signals are applied, so a uniformity test was performed by applying the same pulse train 25 times for each state. Thanks to the excellent CTC variability characteristics of the proposed ECRAM device (Figure 4e), the 16 states were successfully distinguished even with repeated pulse trains, as shown in Figure 4h, making them highly suitable for PRC applications. All 25 current responses for each of the 16 different dynamic patterns are organized in Figure S5 (Supporting Information). It is expected that more states could be distinguished through pulse engineering, such as adjusting the pulse amplitude and width.

In conclusion, the proposed LaF_3/WO_x-based ECRAM exhibits excellent characteristics at the single-device level, including low-power operation and superior reliability. However, for practical application in mobile wearable healthcare devices, array fabrication is necessary for high-density hardware implementation. At this scale, issues such as reliability degradation due to thermal disturbance and unwanted weight updates in half-selected cells inevitably arise.[37,38] We expect that these issues can be
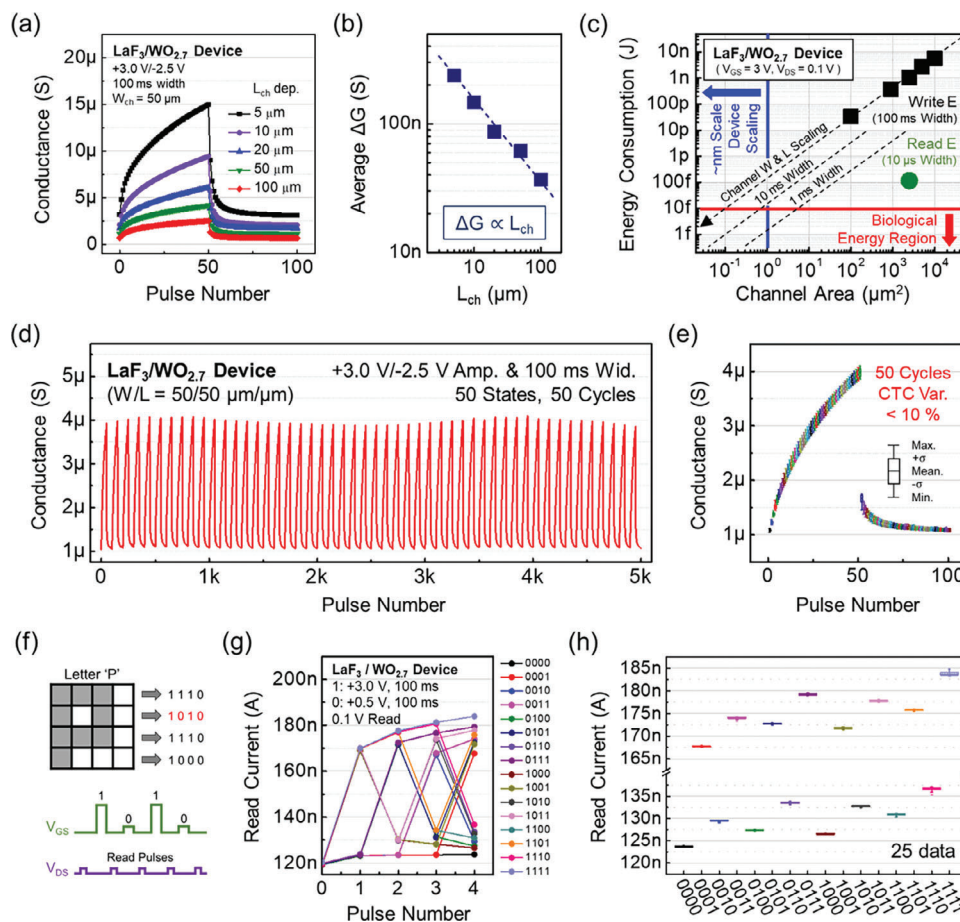
ADVANCED
SCIENCE NEWS

www.advancedsciencenews.com

ADVANCED
ELECTRONIC
MATERIALS

www.advelectronicmat.de

Figure 4. Various device performances of ECRAM with the $LaF_3/WO_{2.7}$ stack. A) Synaptic weight update curves and B) average ΔG under various L_{ch} of the $LaF_3/WO_{2.7}$-based ECRAM. Enhanced operation speed is expected with device size scaling due to the reduction in RC delay. C) Energy consumption for write and read operations in the $LaF_3/WO_{2.7}$ ECRAM, along with scaling trends. The biological energy requirement of 10 fJ spike^{-1} can be achieved through nanometer range scaling of the ECRAM device. D) Cycling endurance characteristics of the $LaF_3/WO_{2.7}$-based ECRAM with consecutive write pulses up to 5×10^3. No conductance degradation was observed during cycling, indicating reliable performance of the $LaF_3/WO_{2.7}$ ECRAM. E) CTC variation of 50 weight update curves of the $LaF_3/WO_{2.7}$ ECRAM. F) Schematic representation of the device operation scheme for image recognition. G) Measured 16 reservoir states of the $LaF_3/WO_{2.7}$-based ECRAM after applying different pulse trains, and H) their distribution. Distinct 16 states with excellent uniformity are achieved due to the superior variability performance.

addressed by introducing temperature compensation circuits[37] and increasing the change in ΔG with respect to write voltage through parameter engineering,[38] respectively.

Finally, to assess the feasibility of the ECRAM-based PRC system for real-world applications, we conducted arrhythmia classification using the MIT-BIH ECG database.[39] The raw ECG signals were first pre-processed to remove noise and normalize the data, ensuring compatibility with the PRC system. The pre-processed signals were then converted into binary spike trains through a quantization process. These binary spike trains were fed in parallel to 15 ECRAM-based memristor nodes, with each node sequentially receiving the data over time (**Figure 5a**). This architecture leverages the temporal dynamics of the input signal, where each memristor node exhibits a unique response pattern based on its intrinsic dynamics and interaction with the input signal. Figure 5b demonstrates that the 15 ECRAM reservoir nodes successfully distinguish between normal and abnormal (arrhythmia) ECG signals. The features extracted from the dynamic response of each reservoir node are transmitted to the output layer,

where they undergo a training process for ECG signal classification. A detailed explanation of the signal pre-processing and feature extraction process is provided in the Supporting Information.

The performance of the proposed ECRAM-based PRC system, consisting of 15 physical nodes and 135 virtual nodes, was compared to that of a traditional 4-layer fully connected DNN, as shown in Figure 5c. A key parameter affecting the PRC system is the CTC variation of the ECRAM nodes, which influences the stability and reliability of their dynamic responses. Although the reservoir's dynamic properties enable it to capture complex temporal patterns, high CTC variation disrupts the consistency of temporal feature encoding, leading to performance degradation when the variation exceeds 10%. Under controlled conditions, with CTC variation maintained below 10%, the ECRAM-based PRC system demonstrated stable and reliable performance, highlighting its robustness for practical applications.

Figure 5d highlights the efficiency of the ECRAM-based PRC system, which achieves classification accuracy comparable to that
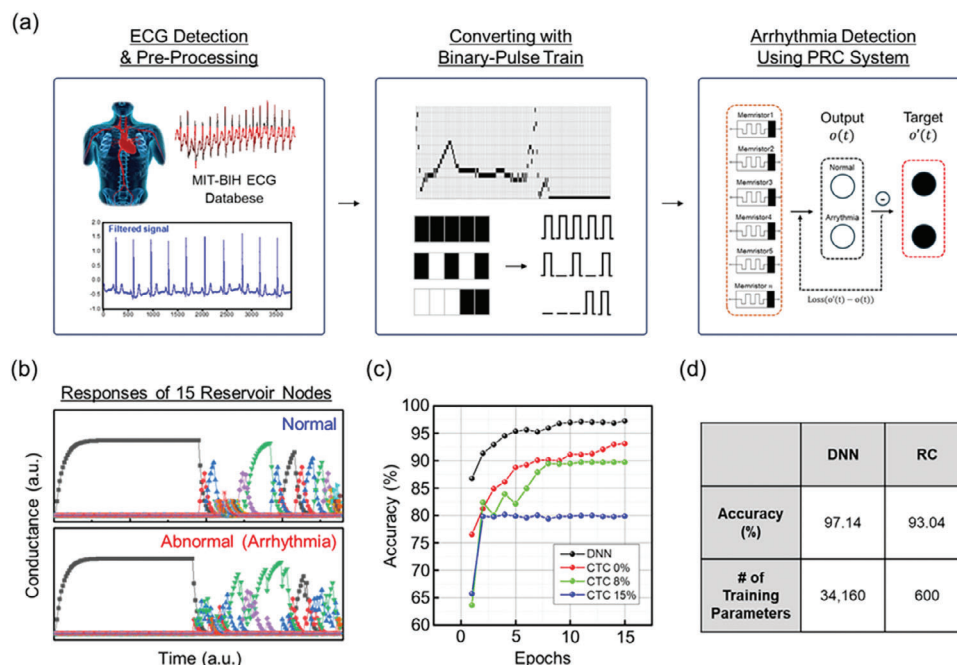
ADVANCED
SCIENCE NEWS

www.advancedsciencenews.com

ADVANCED
ELECTRONIC
MATERIALS

www.advelectronicmat.de

Figure 5. Real-time ECG arrhythmia detection using ECRAM-based PRC system. A) Process flow for detecting ECG anomalies using a dynamic PRC system. The analog ECG signal is quantized into discrete levels proportional to the number of reservoir nodes and converted into a binary pulse train for compatibility with the reservoir input. The reservoir, comprising multiple ECRAM-based nodes, processes the signal dynamically, with each node acting as an independent computational element exhibiting unique responses to the input. B) Reservoir node responses to input signals. The two graphs display the collective responses of 15 reservoir nodes, differentiating normal and arrhythmic conditions through variability in node outputs. C) Classification accuracy for ECG anomaly detection, comparing a fully connected DNN with the ECRAM-based PRC system under varying CTC variability in reservoir nodes. The results highlight the system's sensitivity to CTC variations, emphasizing the importance of optimization. D) Table of classification accuracy with the number of trained synapses. The ECRAM-based PRC system achieves comparable performance to the DNN while using significantly fewer nodes, highlighting its efficiency and robustness in detecting ECG anomalies.

of a fully connected DNN while requiring a significantly fewer number of trainable synapses. This efficiency stems from the reservoir's ability to dynamically encode rich temporal features, thereby reducing the computational burden on the readout layer. By dividing the response of each node into virtual nodes, the PRC expands the feature space without increasing hardware complexity. These results demonstrate the robustness, scalability, and suitability of the PRC system for resource-constrained applications, such as wearable ECG monitoring, where efficiency and simplicity are essential.

3. Conclusion

In conclusion, our study focuses on optimizing LaF_3/WO_x-based ECRAM for advanced bio-potential processing using the PRC system. Utilizing LaF_3 electrolyte with high σ_{ion}, we achieved the non-linear dynamics with STM required for PRC applications. Additionally, by controlling the D_{ion} of the channel layer, we demonstrated tunable time constants within the millisecond range, suitable for bio-potential signals. The device exhibited minimal CTC variation characteristics ($< 10\%$) alongside power-efficient operation (≈ 300 pW spike^{-1}). Moreover, ECG arrhythmia detection tests validated a high classification accuracy (93.04%) in real-time ECG monitoring, highlighting the potential of LaF_3/WO_x-based ECRAM in advanced healthcare applications.

4. Experimental Section

Device Fabrication: All ECRAM devices were fabricated on a thermally grown 100 nm-thick SiO_2 substrate using the RF sputtering process. First, a 25-nm thick WO_x channel layer was deposited via reactive sputtering using a pure W target. To achieve various WO_x stoichiometries, the O_2 gas flow rate was controlled between 3 and 5 sccm, while the Ar gas flow rate was fixed at 30 sccm. Next, 50 nm-thick W source and drain electrodes were deposited at both ends of the WO_x channel layer. Finally, the gate stack consisting of a 15 nm-thick HfO_2 or LaF_3 electrolyte layer, a 25 nm-thick $Gd_{0.1}Ce_{0.9}O_{1.95}$ reservoir layer, and a 50 nm-thick W gate electrode, was sequentially deposited on the active region of the WO_x channel layer. All sputtering processes were conducted at a base pressure of 10^{-6} Torr and a working pressure of 5 mTorr. Except for the WO_x channel layer, all materials were deposited under an Ar gas flow rate of 30 sccm. Regarding sputtering power conditions, LaF_3 was deposited at 20 W, while all other materials were deposited at 100 W. The patterning process was carried out using UV photolithography and a lift-off process.

Material Characterization and Electric Measurements: A high-resolution TEM image was obtained using a JEM-2100F (JEOL). The stoichiometry of the WO_x channel layer was confirmed through XPS spectra using a NEXSA system (Thermo Fisher Scientific, USA). EIS analysis was performed using an impedance analyzer (PalmSens4). All electrical properties were measured by an Agilent B1500A semiconductor device parameter analyzer (Keysight) with waveform generator/fast measurement units (WGFMU). Two WGFMUs were employed for weight update measurements on the fabricated ECRAM device, with one unit connected to the gate electrode for the write operation and the other to the drain electrode for the read operation.

Supporting Information

Acknowledgements

Conflict of Interest

The authors declare no conflict of interest.

Data Availability Statement

The data that support the findings of this study are available from the corresponding author upon reasonable request.

Keywords

[1] V. P. Rachim, W.-Y. Chung, *IEEE Trans. Biomed. Circuits Syst.* **2016**, *10*, 1112.

[2] K. C. Tseng, B.-S. Lin, L.-D. Liao, Y.-T. Wang, Y.-L. Wang, *IEEE Syst. J.* **2013**, *8*, 900.

[3] F. C. Bauer, D. R. Muir, G. Indiveri, *IEEE Trans. Biomed. Circuits Syst.* **2019**, *13*, 1575.

[4] J. M. Bote, J. Recas, F. Rincon, D. Atienza, R. Hermida, *IEEE J. Biomed. health Inf.* **2017**, *22*, 429.

[5] M. Janveja, R. Parmar, M. Tantuway, G. Trivedi, *IEEE Trans. Circuits Syst.* **2022**, *69*, 2281.

[6] S. T. Chandrasekaran, S. P. Bhanushali, I. Banerjee, A. Sanyal, *IEEE Solid-State Circuits Lett.* **2020**, *3*, 290.

[7] Y. Ding, H. Li, X. Liang, M. Vaskeviciute, D. Faccio, H. Heidari, *IEEE Int. Symp. Circuits Syst. (ISCAS)*, IEEE, Singapore, May, **2024**.

[8] D. J. Gauthier, E. Bollt, A. Griffith, W. A. S. Barbosa, *Nat. Commun.* **2021**, *12*, 5564.

[9] G. Tanaka, T. Yamane, J. B. Héroux, R. Nakane, N. Kanazawa, S. Takeda, H. Numata, D. Nakano, A. Hirose, *Neural Networks* **2019**, *115*, 100.

[10] X. Liang, J. Tang, Y. Zhong, B. Gao, H. Qian, H. Wu, *Nat. Electron.* **2024**, *7*, 193.

[11] L. Appeltant, M. C. Soriano, G. Van der Sande, J. Danckaert, S. Massar, J. Dambre, B. Schrauwen, C. R. Mirasso, I. Fischer, *Nat. Commun.* **2011**, *2*, 468.

[12] H. O. Sillin, R. Aguilera, H.-H. Shieh, A. V. Avizienis, M. Aono, A. Z. Stieg, J. K. Gimzewski, *Nanotechnology* **2013**, *24*, 384004.

[13] X. Liang, Y. Zhong, J. Tang, Z. Liu, P. Yao, K. Sun, Q. Zhang, B. Gao, H. Heidari, H. Qian, H. Wu, *Nat. Commun.* **2022**, *13*, 1549.

[14] Y. Zhong, J. Tang, X. Li, X. Liang, Z. Liu, Y. Li, Y. Xi, P. Yao, Z. Hao, B. Gao, H. Qian, H. Wu, *Nat. Electron.* **2022**, *5*, 672.

[15] Y. Zhong, J. Tang, X. Li, B. Gao, H. Qian, H. Wu, *Nat. Commun.* **2021**, *12*, 408.

[16] M. Lee, S. W. Cho, S. J. Kim, J. Y. Kwak, H. Ju, Y. Yi, B.-K. Cheong, S. Lee, *Phys. Rev. Appl.* **2020**, *13*, 064056.

[17] J. Yu, Y. Li, W. Sun, W. Zhang, Z. Gao, D. Dong, Z. Yu, Y. Zhao, J. Lai, Q. Ding, Q. Luo, C. Dou, Q. Zuo, Y. Zhao, S. Chen, R. Zou, H. Chen, Q. Wang, H. Lv, X. Xu, D. Shang, M. Liu, *Symp. VLSI Technology*, IEEE, Kyoto, Japan, June, **2021**.

[18] C.-J. Lee, J.-I. Song, *IEEE Access* **2019**, *7*, 73165.

[19] E. J. Fuller, F. E. Gabaly, F. Leonard, S. Agarwal, S. J. Plimpton, R. B. Jacobs-Gedrim, C. D. James, M. J. Marinella, A. A. Talin, *Adv. Mater.* **2017**, *29*, 1604310.

[20] J. Tang, D. Bishop, S. Kim, M. Copel, T. Gokmen, T. Todorov, S. Shin, K.-T. Lee, P. Solomon, K. Chan, W. Haensch, J. Rozen, *IEEE Int. Electron Devices Meet. (IEDM)*, IEEE, San Francisco, CA, USA, December, **2018**.

[21] R. D. Nikam, J. Lee, K. Lee, H. Hwang, *Small* **2023**, *19*, 2302593.

[22] K. Lee, J. Lee, R. D. Nikam, S. Heo, H. Hwang, *Nanotechnology* **2020**, *31*, 455204.

[23] J. Lee, R. D. Nikam, S. Lim, M. Kwak, H. Hwang, *Nanotechnology* **2020**, *31*, 235203.

[24] S. Kim, T. Todorov, M. Onen, T. Gokmen, D. Bishop, P. Solomon, K.-T. Lee, M. Copel, D. B. Farmer, J. A. Ott, T. Ando, H. Miyazoe, V. Narayanan, J. Rozen, *IEEE Int. Electron Devices Meet. (IEDM)*, IEEE, San Francisco, CA, USA, December, **2019**.

[25] P. Chen, F. Liu, P. Lin, P. Li, Y. Xiao, B. Zhang, G. Pan, *Nat. Commun.* **2023**, *14*, 6184.

[26] R. D. Nikam, M. Kwak, H. Hwang, *Adv. Electron. Mater.* **2021**, *7*, 2100142.

[27] J. Lee, R. D. Nikam, M. Kwak, H. Kwak, S. Kim, H. Hwang, *Adv. Electron. Mater.* **2021**, *7*, 2100219.

[28] J. Lee, R. D. Nikam, M. Kwak, H. Hwang, *ACS Appl. Mater. Interfaces* **2022**, *16*, 45763.

[29] A. Arabacı, M. F. Öksüzömer, *Ceram. Int.* **2012**, *38*, 6509.

[30] D. G. Stroppa, C. J. Dalmaschio, L. Houben, J. Barthel, L. A. Montoro, E. R. Leite, A. J. Ramirez, *Chem.-Eur. J.* **2014**, *20*, 6288.

[31] J. P. Lukaszewicz, N. Miura, N. Yamazoe, *Sens. Actuators, B* **1990**, *1*, 195.

[32] R. A. Huggins, *Ionics* **2002**, *8*, 300.

[33] D. A. Andersson, S. I. Simak, N. V. Skorodumova, I. A. Abrikosov, B. Johansson, *Proc. Natl. Acad. Sci. USA* **2006**, *103*, 3518.

[34] Y. Jiang, J. Liu, *Mater* **2019**, *2*, 30

[35] Y. Jeong, H. Lee, D. G. Ryu, S. H. Cho, G. Lee, S. Kim, S. Kim, Y. S. Lee, *Adv. Electron. Mater.* **2021**, *7*, 2100185.

[36] K. Lee, S. Hwang, D. Kim, J. Yoon, J.-D. Kwon, Y. Kim, H. Hwang, *Adv. Funct. Mater.* **2024**, *34*, 2313802.

[37] C. Lee, M. Kwak, W. Choi, S. Kim, H. Hwang, *IEEE Int. Electron Devices Meet. (IEDM)*, IEEE, San Francisco, CA, USA, December, **2021**.

[38] M. Huang, M. Schwacke, M. Onen, J. del Alamo, J. Li, B. Yildiz, *Adv. Mater.* **2023**, *35*, 2205169.

[39] G. B. Moody, R. G. Mark, *IEEE Eng. Med. Biol. Mag.* **2001**, *20*, 45.